

# Aligned Grid Shaped NiO Nanowires for Humidity Sensing at Room Temperature

**Masoumeh Mohammadi**

University of Kashan

**Mohammad Almasi-Kashi**

University of Kashan

**Somayeh Fardindoost**

Sharif University of Technology

**Azam Irajizad** (✉ [iraji@sharif.edu](mailto:iraji@sharif.edu))

Sharif University of Technology

---

## Research Article

**Keywords:** Aligned NiO nanowires, Electrodeposition, Humidity sensor, Impedance spectroscopy, Ionic conduction

**Posted Date:** December 30th, 2020

**DOI:** <https://doi.org/10.21203/rs.3.rs-135179/v1>

**License:** © ⓘ This work is licensed under a Creative Commons Attribution 4.0 International License.

[Read Full License](#)

---

# Aligned Grid-shaped NiO Nanowires for Humidity Sensing at Room Temperature

Masoumeh Mohammadi <sup>a</sup>, Mohammad Almasi-Kashi <sup>a,b\*</sup>, Somayeh Fardindoost <sup>c</sup> and Azam Iraji zad <sup>c&d\*</sup>

<sup>a</sup>Institute of Nanoscience and Nanotechnology, University of Kashan, 8731753153, Kashan, Iran

<sup>b</sup>Department of Physics, University of Kashan, 8731753153, Kashan, Iran

<sup>c</sup>Department of Physics, Sharif University of Technology, Azadi Street, 11365-9161, Tehran, Iran

<sup>d</sup>Institute for Nanoscience and Nanotechnology, Sharif University of Technology, Azadi Street, 11155-8639, Tehran, Iran

\* E-mail: [almac@kashanu.ac.ir](mailto:almac@kashanu.ac.ir) and [iraji@sharif.edu](mailto:iraji@sharif.edu)

## Abstract

A grid configuration based on the aligned nickel oxide nanowire (NiO NW) for humidity sensing were fabricated through the oxidation of ferromagnetic nickel NWs prepared by a template-assisted electrodeposition process. Their structure and elemental compositions were characterized by field emission scanning electron microscopy (FESEM), X-ray diffraction (XRD), and energy-dispersive X-ray analyses (EDAX). The room-temperature humidity sensing behavior of the NiO NWs was investigated successfully based on DC and AC impedance spectroscopy (IS) method in frequencies range 10 Hz to 2 MHz. The sensors showed excellent humidity sensing characteristics such as a high response of about 66 with rather rapid response-recovery times about 9 and 2 s for 90%RH, and good stability. The equivalent circuits were simulated for impedance responses to humidity in the range of 40% to 90% RH. According to the results, ionic conduction via NW-NW junctions as well as NW-electrode interfaces in the grid configuration is responsible for sensing behavior.

**Keywords:** Aligned NiO nanowires, Electrodeposition, Humidity sensor, Impedance spectroscopy, Ionic conduction.

# 1. Introduction

Sensing and control of humidity are important in a broad spectrum of applications such as agricultural activities, industrial production processes, medical fields, and living environment [1-4]. Therefore, the necessity of microclimate control in different environmental conditions has led to the design and development of various types of humidity sensors [5-7]. The advancements in sensing materials are expected to produce sensors with high sensitivity, fast response-recovery times, low operating temperatures, and good chemical and thermal stability [8-9]. Various kinds of materials such as polymers [10], ceramics [11], graphene [12], carbon nanotubes [13], silica [14], photonic crystals [15], and metal oxides [16] have been studied for humidity sensors. Among them, metal oxides have attracted considerable attention because of their excellent sensing properties, low cost, simple manufacturing process, and obvious operating mechanism [17-18].

The common method to determine environmental relative humidity (RH) is the measurement of changes in conductance or capacitance of these moisture-sensitive materials, originating from the interaction between water molecules and the sample surface [19]. The water molecules in contact with the metal oxide humidity sensor give rise to a change in charge carrier concentrations and alter the resistance and capacitance of the material [19]. Large surface area can significantly improve the response to humidity [20-21]. So, we expect that the one-dimensional (1D) nanowires can provide a much higher surface area, as compared to thin film or bulk materials. As reported for the 1D nanowire arrays, the number of surface active sites for the absorption of water molecules increases, resulting in the overall change of the sensing conduction and increase of the humidity-sensitive characteristic of the sensor [22-25].

Herein, we introduce a humidity sensor based on the grid-shaped arrays of NiO NWs. These sensors were fabricated through oxidation of ferromagnetic Ni NWs prepared by an electrodeposition technique using the anodized aluminum oxide (AAO) template. The template-assisted electrodeposition is a relatively simple and cost-effective technique that can be used for mass production of metal NWs with defined geometry and size [26]. Ni

NWs obtained by this method has a specific diameter and high surface-to-volume ratio with a good crystal structure. On the other hand, the NW grid-shaped arrays is easily accomplished by exerting a uniform magnetic field in two perpendicular directions. To investigate the successful formation of NWs, they were characterized by X-ray diffraction (XRD), optical microscope, field emission scanning electron microscopy (FESEM), and energy-dispersive X-ray (EDX) analyses. The electrical characteristics of NWs in a humid atmosphere such as response and response-recovery times is provided by DC analysis. Impedance spectroscopy is also employed to develop the equivalent circuit model. The proposed circuit is utilized to explain the sensor response mechanism, indicating whether it has resulted from the body of the NWs, junctions, or the electrode-NWs interfaces [27]. In general, the sensor based on the aligned grid-shaped NiO nanowires shows excellent humidity sensing characteristics such as high sensitivity, rapid response-recovery times, and stability.

## **2. Experimental details**

### **2.1. Preparation of the sensors based on aligned NiO NWs**

NiO NWs were prepared by calcination of Ni NWs fabricated by a template-assisted electrodeposition process. In this method, a hard-AAO template was used to fabricate metal NWs [28]. For electrodepositing Ni NWs into nanopores of the template, an aqueous electrolytic bath containing  $\text{NiSO}_4 \cdot 6\text{H}_2\text{O}$  (0.3 M) and boric acid ( $40 \text{ g.l}^{-1}$ ) was used, and the temperature was kept at  $30^\circ\text{C}$ . The electrodeposition process of NWs was performed with a constant reduction voltage of 12 V, an initial oxidation voltage of 10 V, a reduction/oxidation time of 2.4/4.8 ms, and an off-time of 48 ms. During the process, the maximum reduction current density was kept constant at  $50 \text{ mA cm}^{-2}$ . By chemical etching with NaOH solution (2 M) at room temperature for 2 h, the porous alumina membrane was completely removed to finally release the Ni NWs.

The obtained NWs were dispersed in deionized (DI) water to prepare slurry by sonication, followed by distributing it to a glass substrate located in a uniform magnetic

field. The presence of the magnet assisted in the preferential orientation of NWs along the field lines. Accordingly, a grid-shaped structure of NWs was created by placing the glass substrate in two directions perpendicular to the field. The aligned Ni NWs were then converted into the oxide state by calcinating them at a temperature of 500°C for 1 h. The calcination process resulted in better adherence of the NWs onto the substrate while also improving their interfacial contacts and eliminating any organics left by the solvent.

Finally, Ag was sputtered on the array of NiO NWs using a delicately-designed shadow mask with inter-digitized comb-like electrodes (Yar Nikan Saleh Co., Iran). The respective width and length of each finger were about 0.25 and 4 mm. Moreover, the electrode inter-spacing was 0.27 mm. This architecture has hundreds to many thousands of NWs well oriented with many NW–NW junctions and NW–electrode interfaces.

## **2.2. Characterization and measurement techniques**

The wide-angle XRD analysis was performed by an X-ray diffractometer (Panalytical X'Pert Pro) using Cu K $\alpha$  radiation ( $\lambda=1.5418 \text{ \AA}$ ) operating at 40 kV and 30 mA in the range of 35°–80°. The optical image of the sample was obtained from an Optika B-383PLi microscope. FE-SEM images and EDX pattern were recorded using a MIRA3TESCAN-XMU microscope with an accelerating voltage of 15 kV.

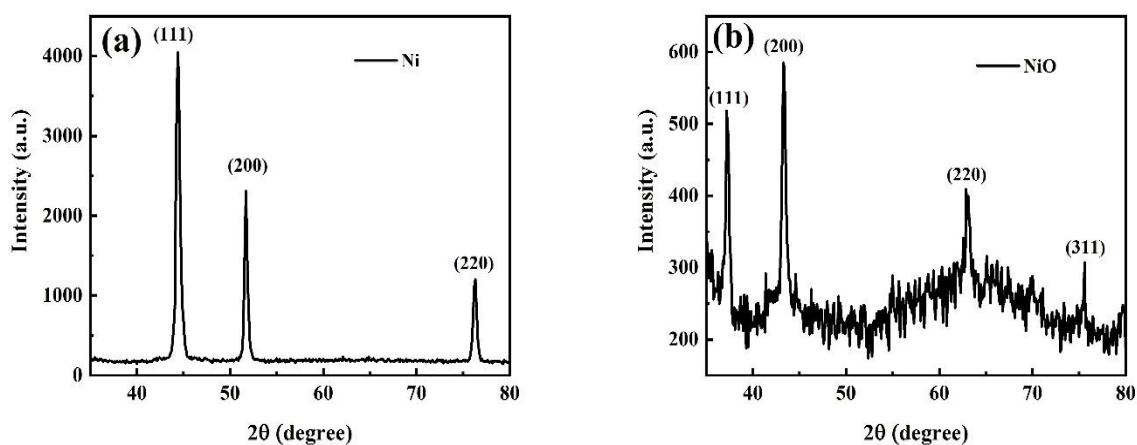
The resistive humidity sensing of the grid-shaped NiO NWs was measured by applying a DC voltage of less than 1 V via a Sanwa Electronic Instrument Co., Ltd. The relative humidity with different percentages ranging from 25% to 90% was generated by the well-controlled flow of dry air into a bowl containing DI water (18 MOhm-cm). The sensor was placed on top of the bowl close to a hygrometer. The impedance spectroscopy sensing performance was tested using an impedance analyzer (Model SI 1260) in a two-point configuration, and a voltage of 50 mV AC signal which overlapped on a constant voltage of less than 1 V DC was applied. The variation in the impedance while the sensor was exposed to humidity was collected in 10 Hz to 2 MHz frequency range. Then the obtained IS data analyzed to figure out the equivalent circuit elements versus RH using a software

package (IS spectrum analyzer software) [29]. All of the sensing measurements were performed at room temperature.

### 3. Results and discussion

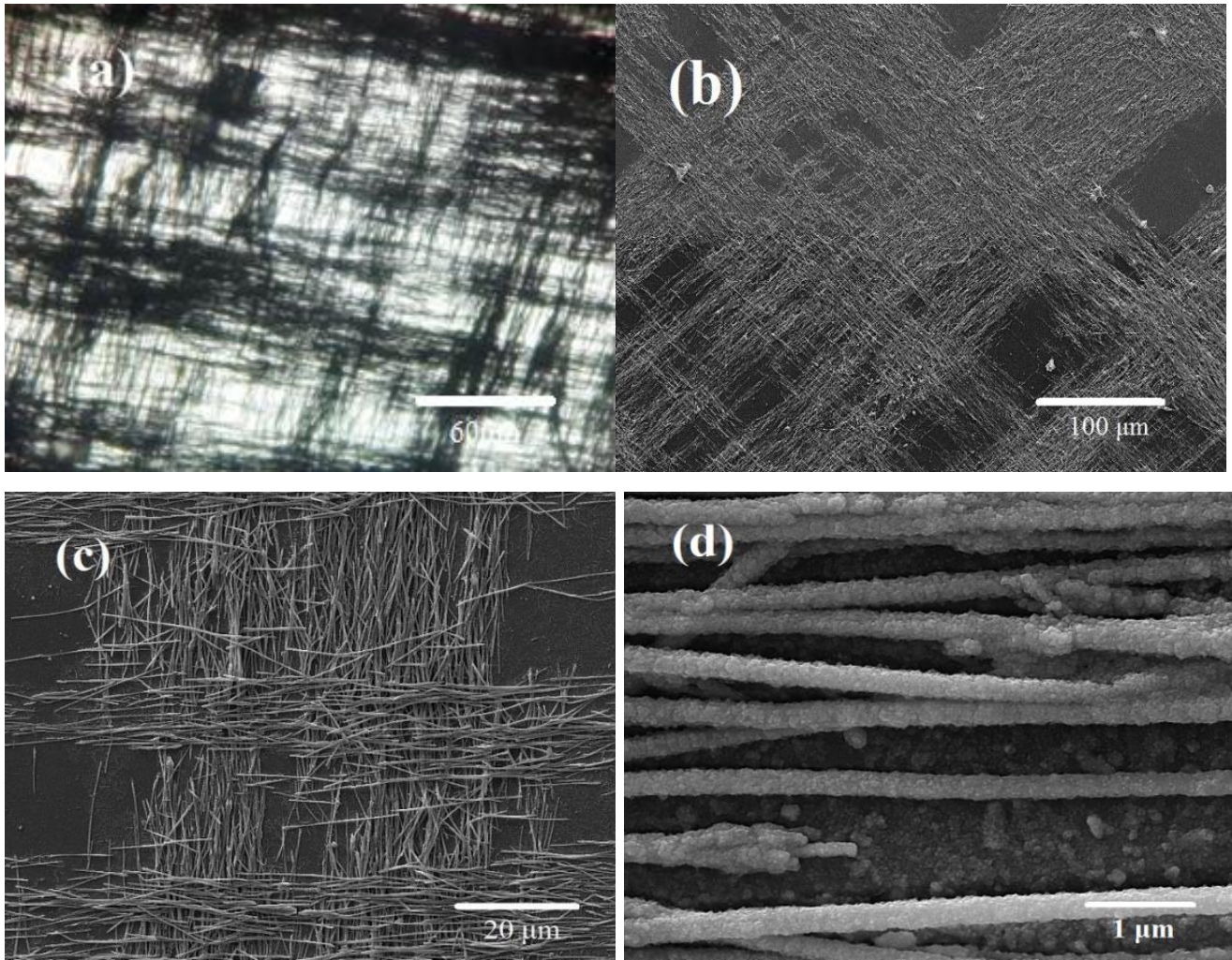
#### 3.1. Structure of the aligned NiO nanowires

Crystal structure and purity of the as-fabricated and calcined Ni NWs were analyzed using the XRD characterization technique. According to the XRD peaks depicted in Fig. 1a, the as-fabricated Ni NWs show three diffraction peaks at  $44.5^\circ$ ,  $51.8^\circ$ , and  $76.4^\circ$  corresponding to (111), (200), and (220) crystal planes, respectively. In Fig. 1b, four diffraction peaks at  $2\theta = 37.4^\circ$ ,  $43.3^\circ$ ,  $62.8^\circ$ , and  $75.44^\circ$  are observed, which correspond to (111), (200), (220), and (311) planes of NiO, respectively. These results indicate that Ni NWs are completely converted into crystalline NiO NWs after the calcination process.



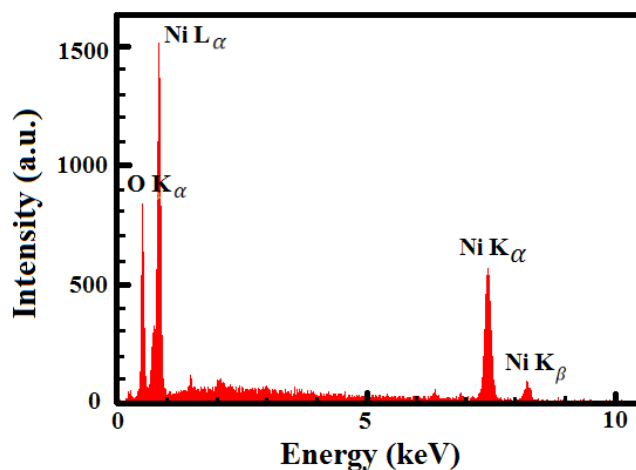
**Fig. 1:** XRD patterns of: (a) as-fabricated Ni, and (b) the calcined Ni (NiO) NWs.

Fig. 2a shows the image taken by an optical microscope after the calcination process. As can be seen, a grid-shaped structure of NiO NWs is created by placing them in two perpendicular directions of a magnetic field. The surface morphology and microstructure of the NiO NWs were also examined by using FESEM. As it is seen from Fig. 2(b–d), the average diameter and length of the NiO NWs are about 270 nm and 25  $\mu\text{m}$ , respectively.



**Fig. 2:** (a) Optical microscope image, and (b-d) FESEM images of aligned NiO NWs.

The elemental compositions of NiO NWs were explored using EDX as shown in Fig. 3. The result shows that the sample contains nickel and oxygen elements.



**Fig. 3:** EDX spectrum of the grid-shaped NiO NWs.

### 3.2. Humidity sensing

To investigate the sensor performance, stable responses of the aligned grid-shaped NiO NWs to humidity ranging from 25% to 90% RH were obtained under a constant DC voltage at room temperature. The resistance changes of the sensor to humidity is represented in Fig. 4a. It is observed that the resistance of the sensor decreases with an increase in RH.

Variation of the responses (defined as  $R_{\text{air}}/ R_{\text{humidity}}$  in which  $R_{\text{air}}$  and  $R_{\text{humidity}}$  are the sensor resistance in the absence and presence of the exposed humidity, respectively [17].) against RH% is shown in Fig. 4b. The plot exhibits an increase in the response of the sensor with the increment in RH. The fitting equation for the lower humidity range can be represented by an exponential function as  $\text{Response} = 0.0129 e^{RH/9.5417} + 0.8208$  with the fit correlation  $R^2 = 0.9963$ . In the above humidity range of 80%, it shows saturation behavior.

Fig. 4c represents typical three consecutive response-recovery cycles for 90% RH indicating fast response and recovery times. As an important characteristic parameter, the response time is defined as the time taken to reach 90% variation in the sample resistance with respect to equilibrium value following an injection of humidity. The recovery time also is defined as the time required for the sample to return to 10 % variation in its

resistance in the air after the removal of the exposed humidity [30]. In our samples, the response and recovery times were around 9 s and 2 s at RH of 90%. Generally, samples presented good stability.

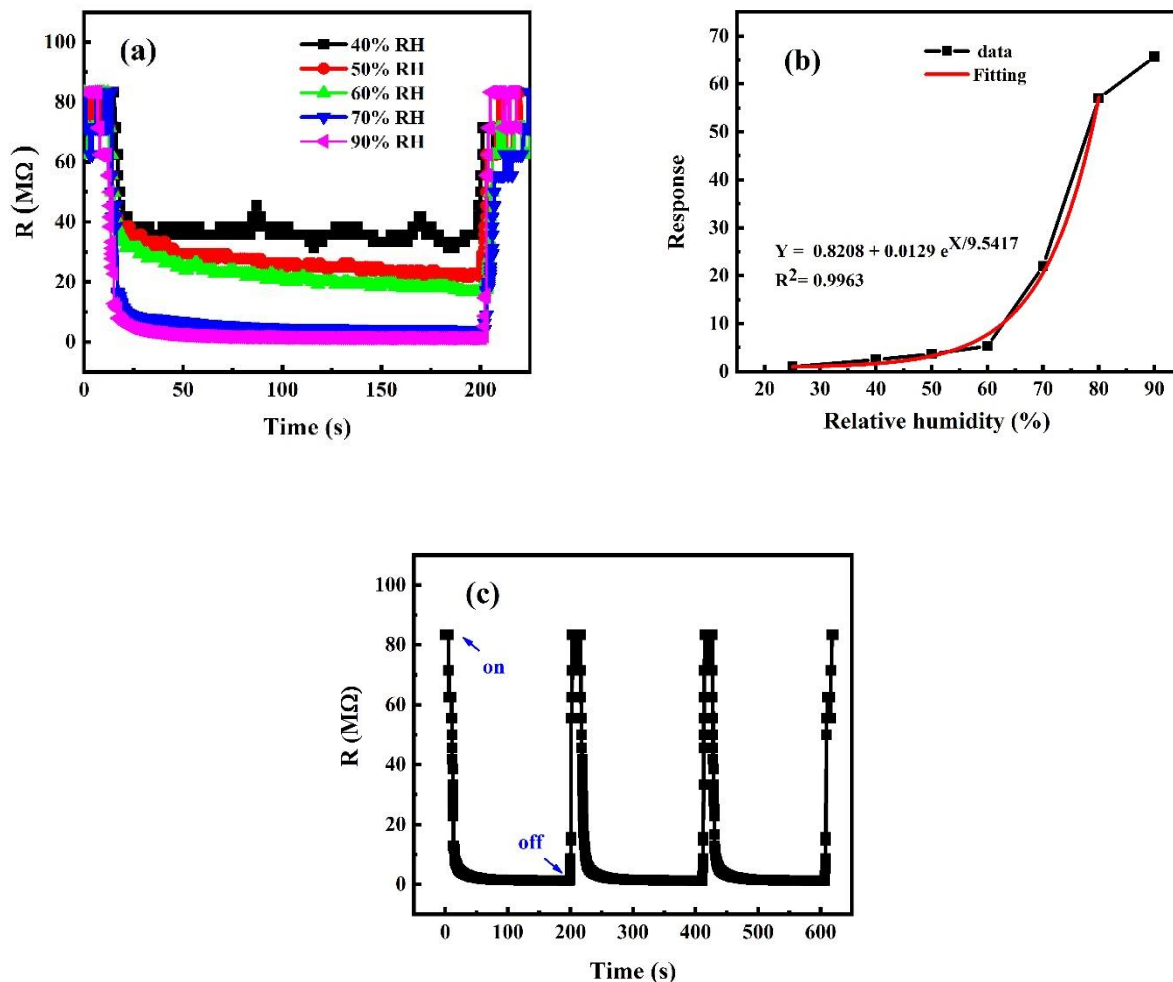


**Fig. 4:** (a) Resistance of the NiO NWs sample as a function of time for different RH, (b) sample response versus relative humidity and (c) typical three consecutive cycles of sample current versus time.

To understand the transport mechanism and different behavior in the response as a function of concentrations at high RH, we perform impedance measurements. The measured signal of the sensor in exposure to humidity includes many components such as the surface and bulk of the sensing material, the wire/wire junctions, and the wires/electrode interfaces. The Nyquist plot of impedance spectroscopy can differentiate the contributions of each of these components [27]. Generally, an equivalent electrical

circuit is used to explain these different processes, which is extremely useful in clarifying the mechanism of the humidity sensor. The response of NiO NWs to humidity investigated by complex impedance spectra [ $Z(\omega) = Z'(\omega) + j Z''(\omega)$ ] is shown in the Nyquist diagrams (Fig. 5a for 40-60% and 5b for 80-90%). The plots show the imaginary part of impedance ( $-Z''$ ) versus the real part ( $Z'$ ) with the centers of semicircles depressed below the real axis so that each point corresponds to a different angular frequency ( $\omega=2\pi f$ ). The equivalent electrical circuits of each semicircle include a resistor (R) in parallel with a constant phase element (CPE; Randle loop). The CPE usually refers to a non-ideal capacitor whose impedance is given by equation (1) [31]:

$$Z_{CPE} = \frac{1}{Q^0(j\omega)^n} \quad (1)$$

Where the constant  $Q^0$  determines the impedance modulus, and the exponent  $n$  is related to the impedance angle which goes from  $0^\circ$  to  $90^\circ$ . In the special case of  $n = 1$  ( $90^\circ$ ),  $Q^0$  becomes C and the CPE acts as a pure capacitor. For  $n = 0$ ,  $Q^0$  becomes  $1/R$  and the element behaves as a pure resistor. If the value of  $n$  is between 0 and 1, CPE would not take the value of either the capacitance or the resistance. In this case, CPE takes a combination of resistor and capacitor [32]. When CPE is in parallel with a resistance, true capacitance values can be calculated from the following equation [31]:

$$C = \frac{(Q^0 \times R)^{1/n}}{R} \quad (2)$$

For nanostructured material, we expect three resistor-capacitor (RC) elements in series, each representing a physical entity of the device. The semicircle plot at lower frequencies is attributed to the material-electrode interface, the middle semicircle to the junctions, and the semicircles at higher frequencies are assigned to the bulk of the material. In practice, the bulk capacitance is usually small compared to that of various interfaces [27]. However

for our samples as shown in Fig. 5(a, b), at low humidity (40–60%), the Nyquist plot shows one semicircle in the whole frequency region, while at high humidity (80–90%), two arcs have appeared (an incomplete depressed arc at low frequency and a nearly perfect semicircle at high frequency). These can be referred to the circuit model in which two frequency-independent resistances,  $R_1$  and  $R_2$ , are in parallel with two constant phase elements,  $CPE_1$ , and  $CPE_2$ , respectively. The fitting parameters for the different RHs are summarized in Table 1. According to the observed range of capacitance values, it is concluded that in the low humidity, the sensor electrical properties originate mainly from NW-NW junctions ( $R_1$  resistance and  $C_1$  capacitance of junctions). Moreover, the electrode-NW interfaces ( $R_2$  resistance and  $C_2$  capacitance of electrode interfaces) can play an important role in the response to the high humidity range.

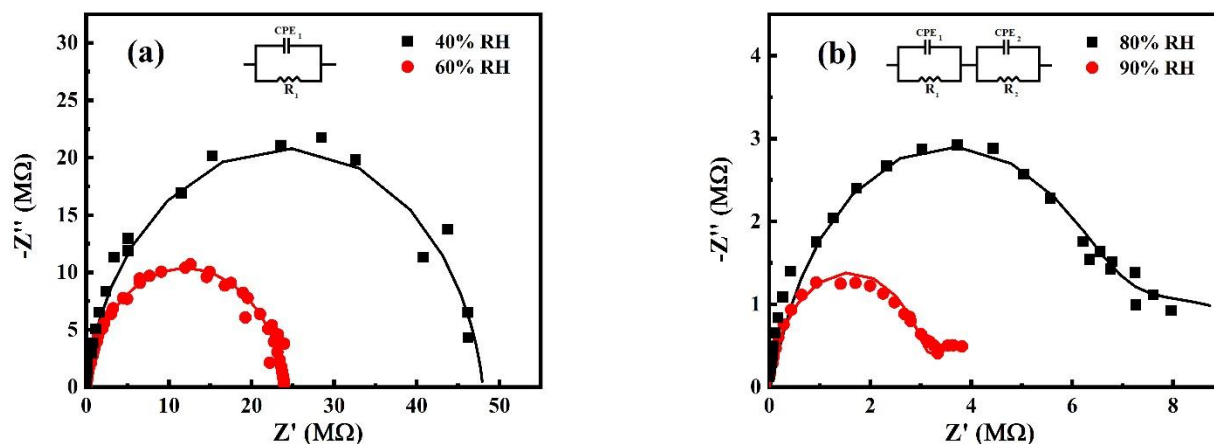


**Fig. 5:** The complex impedance spectra of aligned NiO NWs measured at the RH values of: (a) 40% and 60%, (b) 80% and 90%. For all complex impedance plots, the points and solid lines represent the experimental and fitted data, respectively.

Table 1 indicates that all the calculated resistances are reduced by increasing RH, which can be attributed to the ionic conduction mechanism [33]. Depending on the RH value, both chemisorption and physisorption of the water molecules happen on the NWs surface, at the junctions and interfaces. At low RH, the water molecules chemisorb on the metal cation sites present in the surface of the NWs to make hydroxyl ions by a dissociative mechanism. This chemisorbed layer stays stable and forms the base for further

physisorption of water molecules by the increment of RH at room temperature. As the sensor is exposed to higher RH, the water molecules are physisorbed by hydrogen bonding on the hydroxide surface forming the first physisorbed water layer. By increasing the RH, resistance damped indicates much more water molecules were physically adsorbed forming continuous layer and results in proton hopping between neighboring water molecules. The junctions and interfaces of the nanowires in this grid configuration present a strong electrostatic field, which promotes the water dissociation into  $\text{H}_3\text{O}^+$  and  $\text{OH}^-$ . This dissociation provides protons as charge carriers of the hopping transport. The charge transport occurs when the  $\text{H}_3\text{O}^+$  releases a proton to a nearby  $\text{H}_2\text{O}$  water molecule, ionizing it and forming another  $\text{H}_3\text{O}^+$ , resulting in the hopping of protons from one water molecule to another and decreases the sensor resistance. This process is known as the Grotthuss chain reaction, and it is assumed that it also represents the conduction mechanism in liquid water in higher RHs [34]. In other words, with the increase of the RH, the Grotthuss proton-transfer process takes place, leading to the participation of NW-NW junctions and electrode-NW interfaces in the conduction.

From Table 1, it can also be drawn that the capacitances increase by forming adsorbed layers in the junction and at electrode surfaces of the sensing material with increasing RH to 90%. This means that singly bonded water molecules can form dipoles and reorient freely under an externally applied electric field and thus enhance the electrode and water molecular polarization effects. As seen, the  $C_2$  is far larger than  $C_1$ . It verifies that the electrode polarization effect is much stronger than the water molecular polarization effect. The schematic diagram of NiO NWs sensor is shown in Fig. 6.

**Table 1:** Equivalent circuit model data fittings from aligned NiO NW measurements for different RH%.

RH%	$R_1$ (M $\Omega$ )	$Q_1^0$ ( $10^{-12} \times \Omega^{-1} \text{s}^n$ )	$n_1$	$C_1$ (pF)	$R_2$ (M $\Omega$ )	$Q_2^0$ ( $10^{-9} \times \Omega^{-1} \text{s}^n$ )	$n_2$	$C_2$ (nF)
40	48	5	0.91	2	—	—	—	—
60	24	10.1	0.91	4	—	—	—	—
80	5.9	38	0.91	17	5.1	25	0.45	2.02
90	3.15	83	0.91	37	1.01	15	0.93	10.94

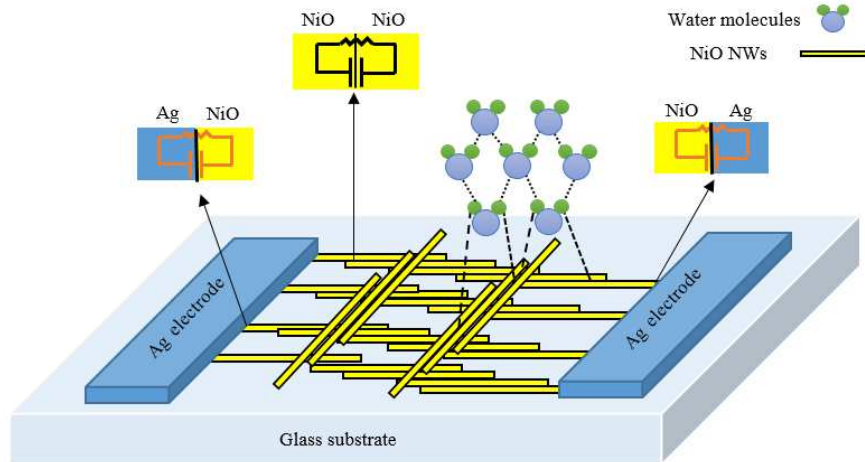


**Fig. 6:** The schematic diagram of NiO NWs sensor's geometry.

Compared to some metal oxide nanostructure-based humidity sensors (see Table 2), our sensor parameters indicate good sensing behavior at room-temperature. This is due to the high surface-to-volume ratio of the nanowires as well as presence of many junctions in an aligned grid-shaped configuration that provide high adsorption sites for water molecules and the large interspaces between the aligned nanowires help water molecules pass quickly through the materials, contribute to the rapid response behavior.

**Table 2:** Humidity sensor performance of this study compared to that of some previous reports.

Sensing material	RH%	Response	Sensitivity (%)	$t_{\text{response}}$ (s)	$t_{\text{recovery}}$ (s)	Reference
ZnO NWs	53.6.	-	-	35.3	32.6	[25]
NiO-SnO <sub>2</sub> nanofibers	83	7.45*	-	18.4	37.2	[35]
ZnO-SnO <sub>2</sub> thin film	92	-	24	21	32	[36]
TiO <sub>2</sub> thin film	90	-	80.85	77.5	3	[37]
SnO <sub>2</sub> thin film	93	55.5*	-	17	2	[38]
Aligned grid-shaped NiO NWs	90	65	98.5	9	2	This work

\*we calculated from their data

## 4. Conclusion

Aligned grid-shaped NiO NWs were fabricated via the electrodeposition technique, followed by a calcination process. The effect of RH on the electrical response of the sensing element was studied based on DC and AC methods. The modeling of impedance spectroscopy results in equivalent circuit and the role of NW-NW junctions and NW-electrode interfaces in response behavior in different RH%. In general, rather good humidity sensing of the sensor described based on sample grid configuration which has many junctions and high surface to volume ratio, providing more active sites and connected media for ion transport and results in short response and recovery times. The high performance NiO nanowires can be used in researches into semiconductor sensors to early detection systems for humidity.

### Author contributions

Azam Irajizad (A.I.) devised the main conceptual idea. Somayeh Fardindoost (S.F.) and Masoumeh Mohammadi (M.M.) planned and carried out the experiments. M.M. fabricated the samples. S.F. and M.M. did the measurements and analyzed the spectra. A.I., Mohammad Almasi-Kashi (M.A.K.), and S.F. helped supervise the findings of this work. M.M. wrote the manuscript with input from all authors. M.M. prepared all figures and tables in the manuscript. All authors discussed the results and contributed to the final manuscript.

### Competing interests

The authors declare no competing interests.

Fig. 1: XRD patterns of: (a) as-fabricated Ni, and (b) the calcined Ni (NiO) NWs.

Fig. 2: (a) Optical microscope image, and (b-d) FESEM images of aligned NiO NWs.

Fig. 3: EDX spectrum of the grid-shaped NiO NWs.

Fig. 4: (a) Resistance of the NiO NWs sample as a function of time for different RH, (b) sample response versus relative humidity and (c) typical three consecutive cycles of sample current versus time.

Fig. 5: The complex impedance spectra of aligned NiO NWs measured at the RH values of: (a) 40% and 60%, (b) 80% and 90%. For all complex impedance plots, the points and solid lines represent the experimental and fitted data, respectively.

Fig. 6: The schematic diagram of NiO NWs sensor's geometry.

## References

- [1] Arularasu, M. V., Harb, M., Vignesh, R. & Sundaram. R. PVDF/ZnO hybrid nanocomposite applied as a resistive humidity sensor. *Surf. Interfaces* **21**, 100780 (2020).
- [2] Qian, J. et al. Positive impedance humidity sensors via single-component materials. *Sci Rep* **6**, 25574 (2016).
- [3] Ismail, A. S. et al. Heterogeneous SnO<sub>2</sub>/ZnO nanoparticulate film: facile synthesis and humidity sensing capability. *Mater. Sci. in Semi. Proc.* **81**, 127-138 (2018).
- [4] Rambabu, A., Singh, D. K., Pant, R., Nanda, K. K. & Krupanidhi, S. B., Self-powered, ultrasensitive, room temperature humidity sensors using SnS<sub>2</sub> nanofilms. *Sci Rep* **10**, 14611 (2020).
- [5] Zhu, K. et al. Improved Response/Recovery Time and Sensitivity of SnSe Nanosheet Humidity Sensor by LiCl Incorporation. *Adv. Electron. Mater.* **6**, 1901330 (2020).
- [6] Cha, X. et al. Superhydrophilic ZnO nanoneedle array: controllable in situ growth on QCM transducer and enhanced humidity sensing properties and mechanism. *Sens. Actuators B: Chem.* **263**, 436-444 (2018).
- [7] Xiao, X. et al. Polysquaraines: novel humidity sensor materials with ultra-high sensitivity and good reversibility. *Sens. Actuators B: Chem.* **255**, 1147-1152 (2018).
- [8] Chen, M. et al. A highly stable optical humidity sensor. *Sens. Actuators B: Chem.* **287**, 329-337 (2019).
- [9] Liu, M. Q., Wang, C. & Kim, N. Y. High-sensitivity and low-hysteresis porous MIM-type capacitive humidity sensor using functional polymer mixed with TiO<sub>2</sub> microparticles. *Sensors*, **17**, 284 (2017).
- [10] Li, X., Zhuang, Z., Qi, D., & Zhao, C. High sensitive and fast response humidity sensor based on polymer composite nanofibers for breath monitoring and non-contact sensing. *Sens. Actuators B: Chem.*, 129239 (2020).
- [11] Sathisha, I. C. et al. Enhanced humidity sensing and magnetic properties of bismuth doped copper ferrites for humidity sensor applications, *J. Alloys Compd.* **848**, 156577 (2020).
- [12] Wang, H. et al. High-performance humidity sensor constructed with vertically aligned graphene arrays on silicon Schottky junctions. *Mater. Lett.* **277**, 128343 (2020).
- [13] Kim, H. S. et al. Carbon nanotubes immobilized on gold electrode as an electrochemical humidity sensor. *Sens. Actuators B: Chem.* **300**, 127049 (2019).
- [14] Qi, R. et al. Capacitive humidity sensors based on mesoporous silica and poly (3, 4-ethylenedioxythiophene) composites. *J. Colloid Interface Sci.* **565**, 592-600 (2020).

- [15] Li, J. X. et al. Fiber temperature and humidity sensor based on photonic crystal fiber coated with graphene oxide. *Optics Communications*, **467**, 125707 (2020).
- [16] Shaheen, K. et al. Electrical, Photocatalytic, and Humidity Sensing Applications of Mixed Metal Oxide Nanocomposites. *ACS omega*, **5**, 7271-7279 (2020).
- [17] Ismail, A. S. et al. Enhanced humidity sensing performance using Sn-doped ZnO nanorod array/SnO<sub>2</sub> nanowire heteronetwork fabricated via two-step solution immersion. *Mater. Lett.* **210**, 258-262 (2018).
- [18] Liu, Y. et al. Hierarchical NiO–CeO nanosheets self-assembly flower-like architecture: heterojunction engineering assisting for high-performance humidity sensor. *J. Mater. Sci.: Mater. Electron.* **31**, 13229-13239 (2020).
- [19] Tomer, V. K., Malik, R., Chaudhary, V., Baruah, A. & Kienle, L. Noble metals-metal oxide mesoporous nanohybrids in humidity and gas sensing applications in *Noble Metal-Metal Oxide Hybrid Nanoparticles* (ed. Holt, S.) 283-302 (Matthew Deans, 2019).
- [20] Wang, G., Wang, Q., Lu, W. & Li, J. Photoelectrochemical study on charge transfer properties of TiO<sub>2</sub>-B nanowires with an application as humidity sensors. *J. Phys. Chem. B.* **110**, 22029-22034 (2006).
- [21] Lei, X., Rui, W., Qi, X., Dan, Z. & Yong, L. Micro humidity sensor with high sensitivity and quick response/recovery based on ZnO/TiO<sub>2</sub> composite nanofibers. *Chin. Phys. Lett.* **28**, 070702 (2011).
- [22] Kim, C. H. et al. Electronic structure of vertically aligned Mn-doped CoFe<sub>2</sub>O<sub>4</sub> nanowires and their application as humidity sensors and photodetectors. *J. Phys. Chem. C.* **113**, 7085–7090 (2009).
- [23] Mohammadi, M., Fardindoost, S., Irajizad, A. & Almasi-Kashi, M. Room temperature selective sensing of aligned Ni nanowires using impedance spectroscopy. *Mater. Res. Express.* **7**, 025044 (2020).
- [24] Hsueh, H. T. et al. CuO nanowire-based humidity sensors prepared on glass substrate. *Sens. Actuators B: Chem.* **156**, 906–911(2011).
- [25] Park, S. et al. Synthesis of self-bridged ZnO nanowires and their humidity sensing properties. *Sens. Actuators B: Chem.* **268**, 293–298 (2018).
- [26] Stępniewski, W. J. & Marco, S. Fabrication of nanowires and nanotubes by anodic alumina template-assisted electrodeposition in *Manufacturing Nanostructures*. (Eds. Waqar, A., Nasar, A.) 321-357 (One central press, 2014).
- [27] Schipani, F. et al. Electrical characterization of semiconductor oxide-based gas sensors using impedance spectroscopy: a review. *Sens. Actuators B: Chem.* **241**, 99–108 (2017).
- [28] Samanifar, S., Kashi, M. A. & Ramazani, A. Study of reversible magnetization in FeCoNi alloy nanowires with different diameters by first order reversal curve (FORC) diagrams. *Physica C.* **548**, 72-74 (2018).
- [29] IS Spectrum Analyser, (n.d.). <http://www.abc.chemistry.bsu.by/vi/analyser/> (2020).
- [30] Yadav, S. et al. Facile synthesis of molybdenum disulfide (MoS<sub>2</sub>) quantum dots and its application in humidity sensing. *Nanotechnology*, **30** (2019) 295501.
- [31] Sanchez, M., Rincon, M. E. & Lopez, R. A. G. Anomalous sensor response of TiO<sub>2</sub> films: electrochemical impedance spectroscopy and ab initio studies. *J. Phys. Chem. C.* **113**, 21635–21641 (2009).

- [32] Mohanty, V., Cheruku, R., Vijayan, L. & Govindaraj, G. Ce-substituted lithium ferrite: preparation and electrical relaxation studies. *J. Mater. Sci. Technol.* **30**, 335-341 (2014).
- [33] Traversa, E., Ceramic sensors for humidity detection: the state-of-the-art and future developments. *Sens. Actuators B Chem.*, **23**,135-156 (1995).
- [34] Pan, M., Sheng, J., Liu, J., Shi, Z. & Jiu, L. Design and Verification of Humidity Sensors Based on Magnesium Oxide Micro-Arc Oxidation Film Layers. *Sensors*, **20**, 1736 (2020).
- [35] Pascariu, P. et al. Microstructure, electrical and humidity sensor properties of electrospun NiO–SnO<sub>2</sub> nanofibers. *Sens. Actuators B: Chem.* **222**, 1024-1031 (2016).
- [36] Velumani, M., Meher, S. R. & Alex. Z. C. Impedometric humidity sensing characteristics of SnO<sub>2</sub> thin films and SnO<sub>2</sub>–ZnO composite thin films grown by magnetron sputtering. *J. Mater. Sci.: Mater. Electron.* **29**, 3999-4010 (2018).
- [37] Gapale, D. L., Arote, S. A., Palve, B. M., & Borse, R. Y. Influence of precursor solution concentration on the structural, optical and humidity sensing properties of spray-deposited TiO<sub>2</sub> thin films. *J. Semicond.* **39**, 122003 (2018).
- [38] Racheva, T. M., & Critchlow, G. W. SnO<sub>2</sub> thin films prepared by the sol-gel process. *Thin Solid Films.* **292**, 299-302 (1997).

**Table 1:** Equivalent circuit model data fittings from aligned NiO NW measurements for different RH%.

RH%	R <sub>1</sub> (MΩ)	Q <sub>1</sub> (10 <sup>-12</sup> × Ω <sup>-1</sup> s <sup>n</sup> )	n <sub>1</sub>	C <sub>1</sub> (pF)	R <sub>2</sub> (MΩ)	Q <sub>2</sub> (10 <sup>-9</sup> × Ω <sup>-1</sup> s <sup>n</sup> )	n <sub>2</sub>	C <sub>2</sub> (nF)
40	48	5	0.91	2	–	–	–	–
60	24	10.1	0.91	4	–	–	–	–
80	5.9	38	0.91	17	5.1	25	0.45	2.02
90	3.15	83	0.91	37	1.01	15	0.93	10.94

**Table 2:** Humidity sensor performance of this study compared to that of some previous reports.

Sensing material	RH%	Response	Sensitivity (%)	t <sub>response</sub> (s)	t <sub>recovery</sub> (s)	Reference
ZnO NWs	53.6.	-	-	35.3	32.6	[25]
NiO–SnO <sub>2</sub> nanofibers	83	7.45*	-	18.4	37.2	[35]
ZnO-SnO <sub>2</sub> thin film	92	-	24	21	32	[36]
TiO <sub>2</sub> thin film	90	-	80.85	77.5	3	[37]
SnO <sub>2</sub> thin film	93	55.5*	-	17	2	[38]
Aligned grid-shaped NiO NWs	90	65	98.5	9	2	This work

\*we calculated from their data

# Figures

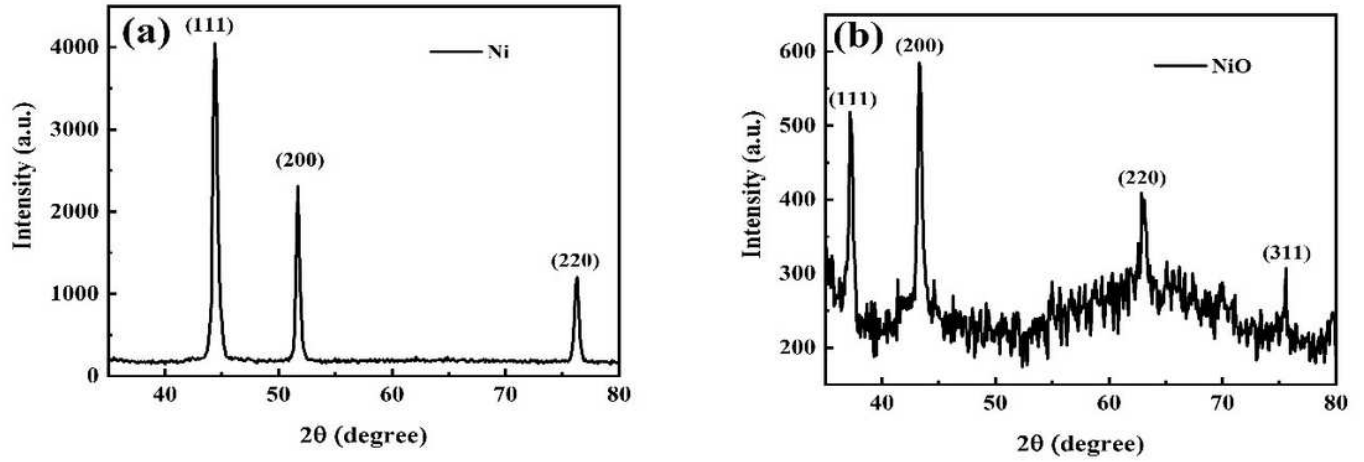
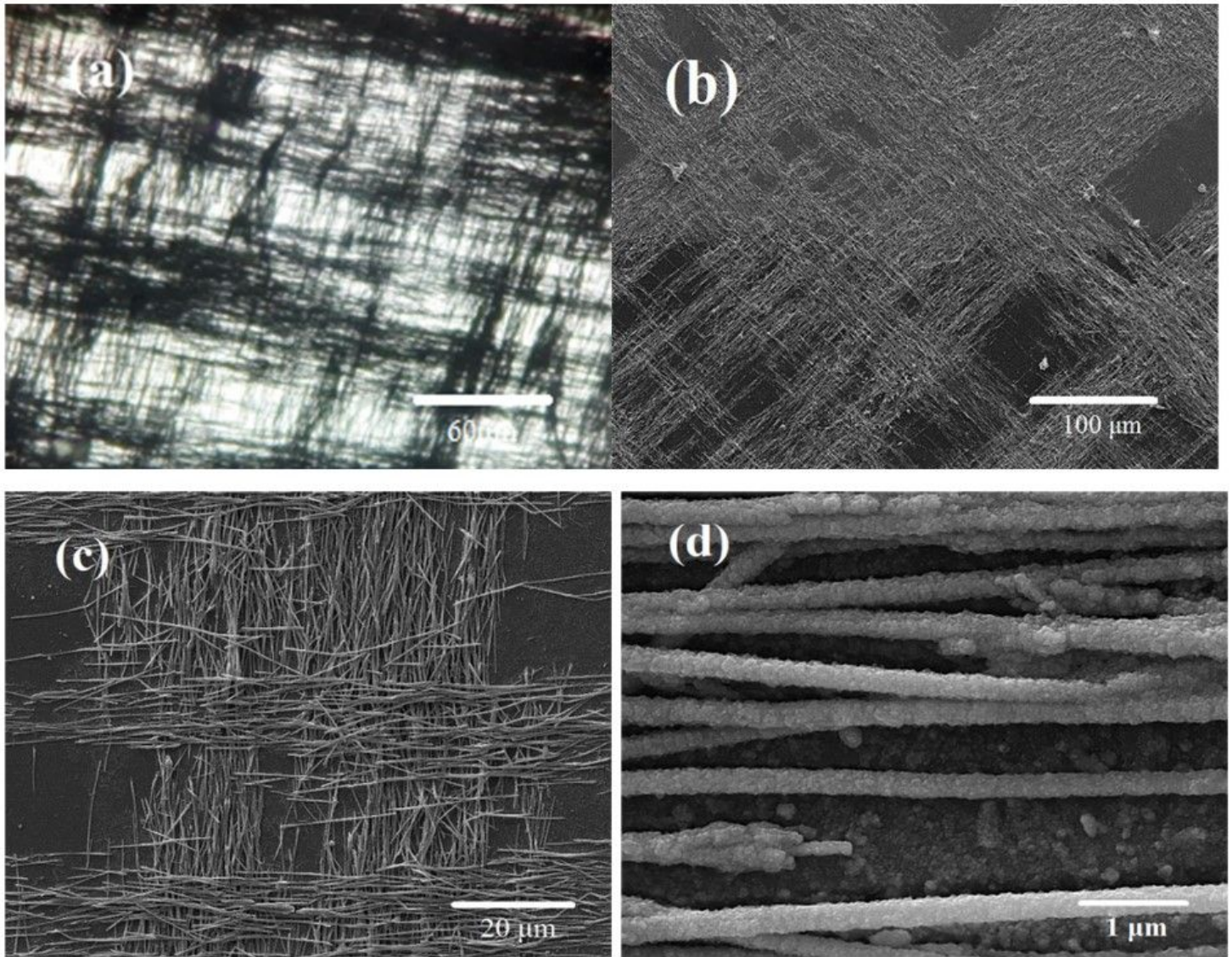


Figure 1

XRD patterns of: (a) as-fabricated Ni, and (b) the calcined Ni (NiO) NWs.



**Figure 2**

(a) Optical microscope image, and (b-d) FESEM images of aligned NiO NWs.

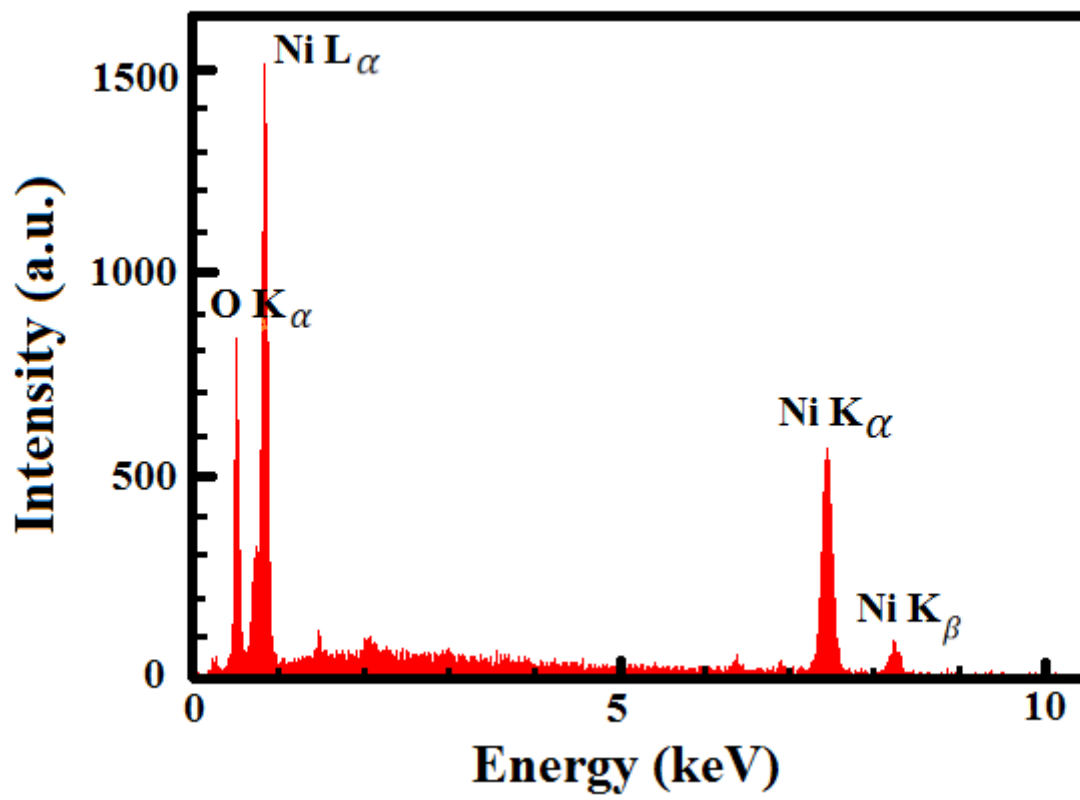


Figure 3

EDX spectrum of the grid-shaped NiO NWs.

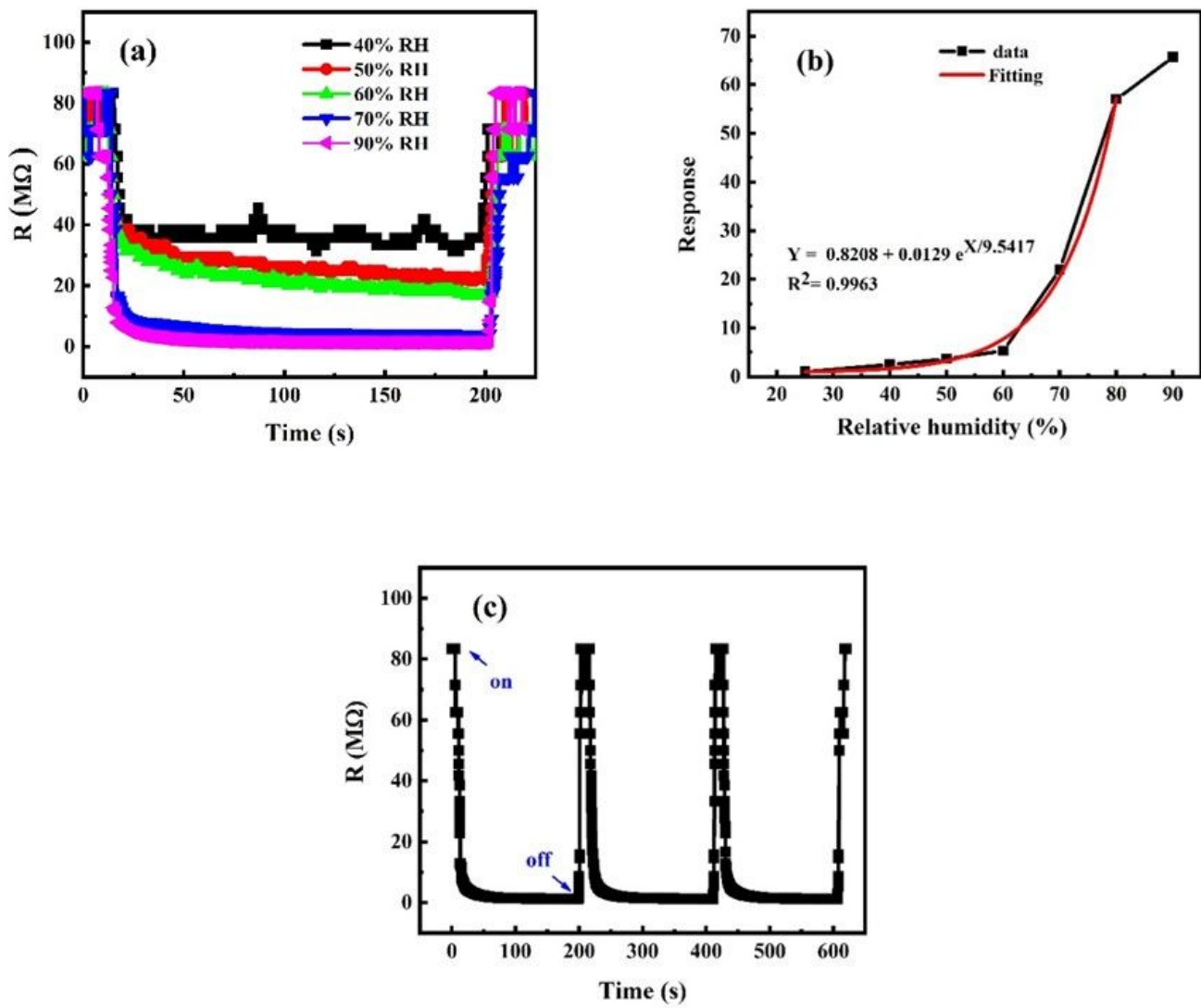


Figure 4

(a) Resistance of the NiO NWs sample as a function of time for different RH, (b) sample response versus relative humidity and (c) typical three consecutive cycles of sample current versus time.

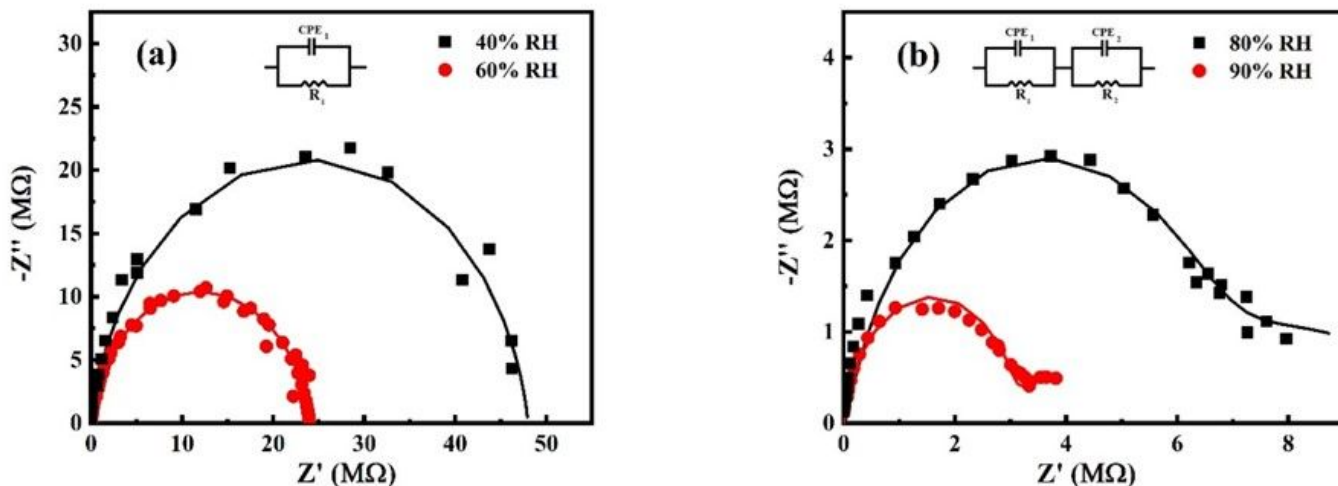


Figure 5

The complex impedance spectra of aligned NiO NWs measured at the RH values of: (a) 40% and 60%, (b) 80% and 90%. For all complex impedance plots, the points and solid lines represent the experimental and fitted data, respectively.

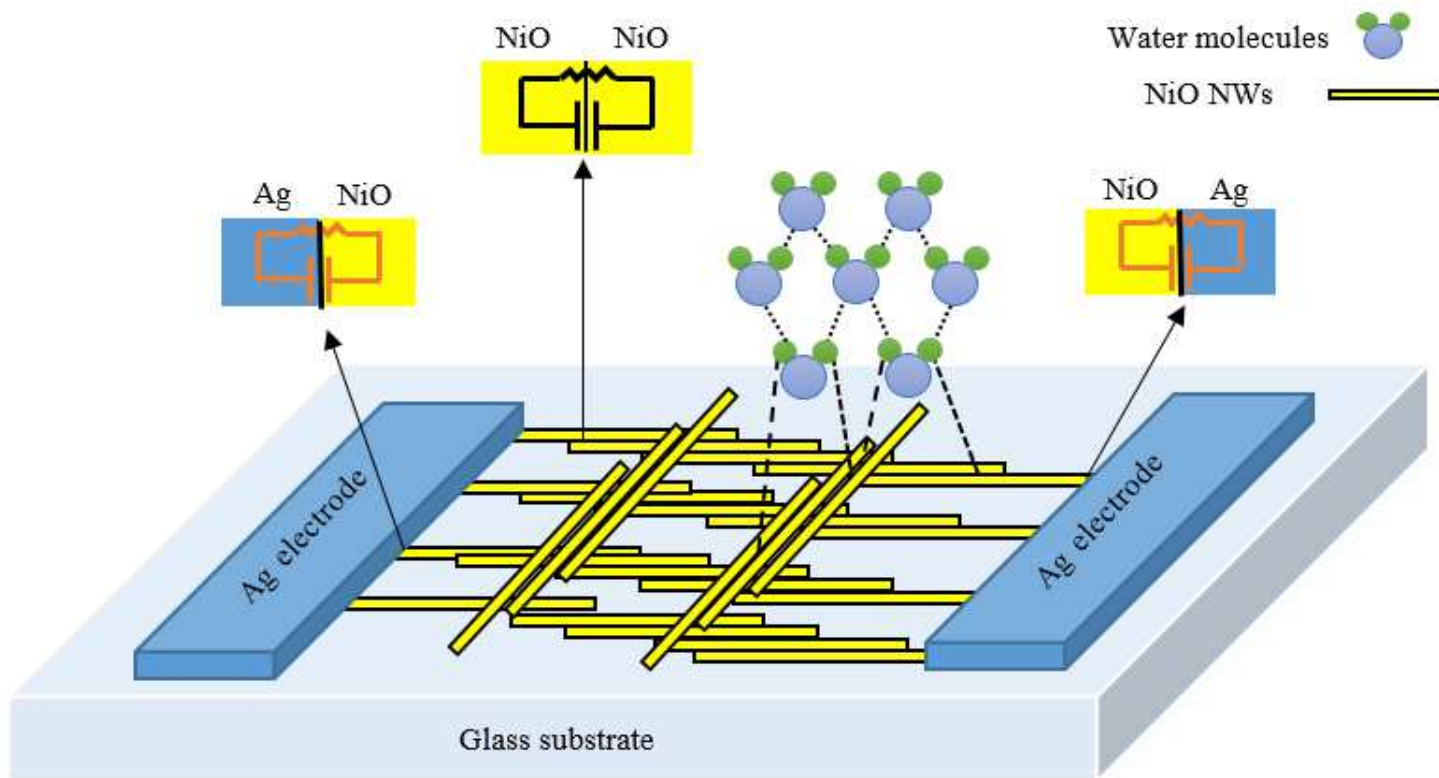


Figure 6

The schematic diagram of NiO NWs sensor's geometry.